Simulation of seismograms in a 2-D viscoelastic Earth by pseudospectral methods

José M. Carcione[1], Hans B. Helle[2], Géza Seriani[1] and Milton P. Plasencia Linares[3]

[1] *Istituto Nazionale di Oceanografia e di Geofisica Sperimentale (OGS), Trieste, Italy*
[2] *Norsk Hydro a.s., 0 & E Research Centre, Bergen, Norway*
[3] *Depto. de Sismología, Fac. de Ciencias Astronómicas y Geofísicas, Universidad Nacional de La Plata, La Plata, Argentina*

RESUMEN

El algoritmo de modulación seudoespectral es mejorado y aplicado a la simulación de sismogramas generados por sismos oceánicos y continentales, como atención a la atenuación y a la modelación explícita de condiciones a la frontera en el fondo oceánico y a la simulación de la ventana de Rayleigh y la propagación en interfases. El algoritmo se basa en los operadores diferenciales de Fourier y de Chebyshev con una técnica de decomposición de dominios, una malla para el fluido y otra para el sólido. Para la propagación se usa una relación de esfuerzo-deformación basada en variables de memoria. Entre los fenómenos modelados se incluyen las ondas de Scholte, las ondas evanescentes de Rayleigh y los modos dispersivos, así como la ventana de Rayleigh, un mínimo del coeficiente de reflexión en el fondo oceánico que nunca ha sido simulado con métodos directos. Hemos modelado los modos de Rayleigh (principalmente M_{11}) y las ondas acopladas Rayleigh-Scholte, resolviendo la relación de dispersión para casos simples. Se modeló también efectos de inhomogeneidades aleatorias en la corteza y manto mediante una función de autocovarianza tipo von Kármán que simula los efectos de dispersión de ondas.

El programa bidimensional permite una variación material general y una caracterización completa y exacta de la respuesta para sismos oceánicos y continentales. Se desarrolla un ejemplo para un sismograma originado en la región del Atlántico Sur.

PALABRAS CLAVE: Sismograma, sismo, atenuación, modelado, ondas de Rayleigh, ondas de Scholte, ventana de Rayleigh.

ABSTRACT

Using an improved global pseudospectral modeling algorithm we synthesize seismograms generated by oceanic and continental earthquakes. Attention is given to attenuation, to explicit modeling of boundary conditions at the ocean-bottom interface, simulation of the Rayleigh window and interface-wave propagation. The algorithm is based on Fourier and Chebyshev differential operators and a domain-decomposition technique - one grid for the fluid and another grid for the solid. Wave propagation in the oceanic and continent crusts and mantle is modeled by using a viscoelastic stress-strain relation based on memory variables.

The main physical phenomena associated with an ocean-crust system are modeled, including Scholte waves, leaking Rayleigh waves, dispersive modes, and the Rayleigh-window phenomenon due to a minimum in the reflection coefficient of the ocean bottom, which has not been simulated with direct methods. In particular, we model Rayleigh modes (mainly the M_{11} mode), and coupled Rayleigh-Scholte waves, for which the dispersion relation is solved in simple cases. Also, we model the effects of random inhomogeneities in the crust and mantle by using a von Kármán autocovariance probability function, which simulates scattering-Q-effects.

The 2-D modeling code allows general material variability, and a complete and accurate characterization of the seismic response of oceanic and continental earthquakes. A synthetic seismogram for an earthquake in the South Atlantic region is provided.

KEY WORDS: Seismogram, earthquake, attenuation, modeling, Rayleigh waves, Scholte waves, Rayleigh window.

INTRODUCTION

Understanding the physics of wave propagation of earthquakes is essential for a proper interpretation of the seismic properties and geometrical features of the continental and oceanic crusts. The dispersion equation of simple systems, such as an oceanic layer overlying an elastic lossless half-space, can be solved using analytical methods (Biot, 1952; Ewing *et al.*, 1957, p. 156). More complicated situa- tions, involving arbitrary velocity variations, fluid-solid interfaces and attenuation with complex mode coupling (*e.g.,* Ben-Menahem, 1965; Butler and Lomnitz, 2002; Lomnitz *et al.*, 2002), require an accurate numerical modeling algorithm using direct grid methods, so that general variability of the seismic properties can be modeled (see Carcione, 2001, Chapter 8; and Carcione *et al.*, 2002 for a review). Normal-mode coupling (Capdeville *et al.*, 2000), Galerkin methods (Takeuchi *et al.*, 2000), finite differences (Thomas *et al.*,

2000), and global pseudospectral methods (Coutel and Mora, 1998; Igel, 1999) have been used to treat this problem. Recently, Komatitsch and Tromp (2002a,b) developed a three-dimensional spectral-element approach for the simulation of global seismic propagation throughout the globe. Their algorithm includes anisotropy, attenuation based on memory variables (Emmerich and Korn, 1987; Carcione, 2001, p. 110), the effects of 3-D mantle and crustal models, the oceans, the Earth's ellipticity, topographic features, bathymetry, rotation and self-gravitation. The effect of the ocean is based upon an equivalent surface load integral, which does not require meshing, but this approximation breaks down for short periods, typically below 5 s. (The oceans are assumed to be incompressible.) Komatitsch and Tromp use Legendre-basis functions in contrast to Priolo *et al.* (1994), Seriani (1998) and Priolo (1999), who use Chebyshev-basis functions.

For wave propagation in the oceanic crust, in particular, for modeling interface waves and the Rayleigh-window effect, we explicitly model the slip boundary condition at the ocean-bottom interface by using a domain-decomposition technique and pseudospectral methods. One mesh is used to discretize the ocean and another the crust. For each mesh, a method developed by Carcione (1992) is used. It involves a Fourier method along the interface direction and Chebyshev along the direction perpendicular to the surface, or the ocean-bottom interface. Thus, the grid points are equally spaced in the horizontal direction and are given by the Gauss-Lobatto collocation points in the vertical direction (denser at the edges of the mesh). The domain-decomposition approach for viscoelastic waves is illustrated in Carcione (1991, 1994a). Modeling examples are given in Kessler and Kosloff (1991) and Tessmer *et al.* (1992) for elastic media, and in Carcione (1996) for viscoelastic media. We consider a flat interface, but the algorithm can be extended to model topographic features of the ocean bottom by using a mapping transformation (*e.g.,* Carcione, 1994b).

We first verify the domain decomposition by comparing the numerical and analytical solutions in a lossless model. A test of the anelastic model simulates the Rayleigh-window phenomenon. This is a viscoelastic effect, implying that the energy incident on the boundary at angles within that window is substantially transmitted. Borcherdt *et al.* (1986) present theoretical and experimental results for a water-stainless steel interface (*e.g.,* Carcione, 2001, p. 214). To our knowledge, the Rayleigh window has not previously been simulated with direct grid methods.

The modeling is then used to model propagation in the oceanic and continental crusts. The physics is first illustrated for a homogeneous ocean bottom (Biot, 1952). Interface waves are dispersive and several modes can propagate. The fundamental mode is a Scholte wave at short wavelengths in terms of the water depth, and becomes a Rayleigh wave at long wavelengths. We model the propagation of the fundamental Rayleigh mode in the continental crust, the M_{11} mode. As a final example we show a synthetic seismograms generated by an earthquake in the South Atlantic; lateral variations in seismic velocity are modeled. Since the coherency of the wave field can be degraded by the heterogeneous nature of the crust at small scales, we use a spatially isotropic von Kármán autocovariance probability function of high fractal dimension to simulate scattering-Q effects (Holliger, 1997). We consider correlation lengths of the order of a few km and a standard deviation of the velocity fluctuations of a few percent.

EQUATION OF MOTION

The time-domain equations for propagation in a heterogeneous viscoelastic medium can be found in Carcione (2001, p. 110). The anelasticity is described by the standard linear solid, also called the Zener model, that gives relaxation and creep functions in agreement with experimental results (Zener, 1948).

The two-dimensional velocity-stress equations for anelastic propagation in the (x, z)-plane, assigning one relaxation mechanism to dilatational anelastic deformations ($\nu = 1$) and one relaxation mechanism to shear anelastic deformations ($\nu = 2$), can be expressed by

i) Euler-Newton's equations:

$$\dot{v}_x = \frac{1}{\rho}(\sigma_{xx,x} + \sigma_{xz,z}) + f_x, \tag{1}$$

and

$$\dot{v}_z = \frac{1}{\rho}(\sigma_{xz,x} + \sigma_{zz,z}) + f_z, \tag{2}$$

where v_x and v_z are the particle velocities, σ_{xx}, σ_{zz} and σ_{xz} are the stress components, ρ is the density and f_x and f_z are single body forces. A dot above a variable denotes time differentiation.

ii) Constitutive equations:

$$\dot{\sigma}_{xx} = k(v_{x,x} + v_{z,z} + e_1) + \mu(v_{x,x} - v_{z,z} + e_2) + M_{xx}, \tag{3}$$

$$\dot{\sigma}_{zz} = k(v_{x,x} + v_{z,z} + e_1) - \mu(v_{x,x} - v_{z,z} + e_2) + M_{zz}, \tag{4}$$

and

$$\dot{\sigma}_{xz} = \mu(v_{x,z} + v_{z,x} + e_3) + M_{xz}, \tag{5}$$

where e_1, e_2 and e_3 are memory variables, M_{xx}, M_{zz} and M_{xz} are moment tensor components defining the radiation patterns of the source mechanism, and k and μ are the unrelaxed (high-frequency) bulk and shear moduli, respectively.

iii) Memory variable equations:

$$\dot{e}_1 = \left(\frac{1}{\tau_\in^{(1)}} - \frac{1}{\tau_\sigma^{(1)}} \right)(v_{x,x} + v_{z,z}) - \frac{e_1}{\tau_\sigma^{(1)}} \qquad (6)$$

$$\dot{e}_2 = \left(\frac{1}{\tau_\in^{(2)}} - \frac{1}{\tau_\sigma^{(2)}} \right)(v_{x,x} + v_{z,z}) - \frac{e_2}{\tau_\sigma^{(2)}} \qquad (7)$$

and

$$\dot{e}_3 = \left(\frac{1}{\tau_\in^{(2)}} - \frac{1}{\tau_\sigma^{(2)}} \right)(v_{x,z} + v_{z,x}) - \frac{e_3}{\tau_\sigma^{(2)}} \qquad (8)$$

where $\tau_\sigma^{(v)}$ and $\tau_\in^{(v)}$ are material relaxation times, corresponding to dilatational ($v = 1$) and shear ($v = 2$) deformations. We recall that in a two-dimensional world, $\mu = \rho V_S^2$ and $k = \rho(V_P^2 - V_S^2)$, where V_P an V_S are the compressional- and shear-wave unrelaxed velocities.

The equations for the viscoacoustic medium are obtained from (1) - (8) by setting $\sigma_{xx} = \sigma_{zz} \equiv -p$, $\sigma_{xz} = 0$ and $\mu = 0$. Then, the equations of motion are

$$\dot{v}_x = \frac{\sigma_{,x}}{\rho} + f_x, \qquad (9)$$

and

$$\dot{v}_z = \frac{\sigma_{,z}}{\rho} + f_z, \qquad (10)$$

where

$$\dot{\sigma} = k(v_{x,x} + v_{z,z} + e_1), \qquad (11)$$

together with the memory-variable equation (6). The introduction of additional differential equations for the memory variables avoids numerical computation of the convolution integrals involved in the viscoelastic stress-strain relation. Physically, the stress at time t depends on past values of the strain field, and this information is contained in the memory (hidden) variables. The extension of the theory to many dissipation mechanisms is straightforward (Carcione, 2001, p. 210). Using many mechanisms whose peak relaxation frequencies are equally spaced on the log-frequency axis, it is possible to model a constant Q stress-strain relation.

Complex velocities

The complex velocities of body waves, v_P and v_S, are the key quantities to obtain the phase velocities and attenuation factors. They are defined by

$$\rho v_P^2(\omega) = kM_1(\omega) + \mu M_2(\omega), \quad \text{and} \quad \rho v_S^2(\omega) = \mu M_2(\omega) \qquad (12)$$

(Carcione, 2001, p. 65, 85), where ω is the angular frequency, and

$$M_v = \frac{\tau_\sigma^{(v)}}{\tau_\in^{(v)}} \left(\frac{1 + i\omega\tau_\in^{(v)}}{1 + i\omega\tau_\sigma^{(v)}} \right), \quad v = 1, 2 \qquad (13)$$

are the Zener complex moduli.

The relaxation times can be expressed as

$$\tau_\in^{(v)} = \frac{\tau_0}{Q_{0v}} \left[\sqrt{Q_{0v}^2 + 1} + 1 \right], \quad \tau_\sigma^{(v)} = \tau_\in^{(v)} - \frac{2\tau_0}{Q_{0v}}, \qquad (14)$$

where τ_0 is a relaxation time such that $1/\tau_0$ is the center angular frequency of the relaxation peak and Q_{0v} are the minimum quality factors at this center frequency.

The quality factor, Q_{01}, associated with the bulk modulus, is obtained from the relation

$$\frac{1 + \sigma}{Q_{01}} = \frac{3(1 - \sigma)}{Q_{0P}} - \frac{2(1 - 2\sigma)}{Q_{02}}, \quad \sigma = \frac{V_P^2 - 2V_S^2}{2(V_P^2 - 2V_S^2)} \qquad (15)$$

(Winkler and Nur, 1979), where Q_{0P} is a parameter related to the P-wave quality factor and σ is Poisson's ratio.

Similarly, the complex velocity for the viscoacoustic medium is

$$\rho v_P^2(\omega) = kM_1(\omega) . \qquad (16)$$

PROPAGATION CHARACTERISTICS

A general plane wave solution for the particle velocity field $\mathbf{v} = (v_x, v_z)$ is

$$\mathbf{v} = i\omega \mathbf{U} \exp [i\omega(t - s_x x - s_z z)], \qquad (17)$$

where s_x and s_z are the components of the complex slowness vector, t is the time variable and $\mathbf{U}$ is a complex vector. For homogeneous viscoelastic waves, the directions of propagation and attenuation coincide and

$$s_x = \sin \theta / v; \quad s_z = \cos \theta / v, \qquad (18)$$

where θ is the propagation angle, measured with respect to the z-axis, and $v = 1/s$ is the complex velocity.

For homogeneous waves in isotropic media, the phase velocity and attenuation factors are given by

$$v_p = \left[\text{Re}\left(\frac{1}{v} \right) \right]^{-1}, \qquad (19)$$

$$\alpha = -\omega \, \text{Im}\left(\frac{1}{\upsilon}\right), \tag{20}$$

the group velocity is

$$\upsilon_g = \upsilon_p \left[1 - \frac{\omega}{\upsilon_p} \frac{d\upsilon_p}{d\omega}\right]^{-1}, \tag{21}$$

and the quality factor is given by

$$Q = \frac{\text{Re}(\upsilon^2)}{\text{Im}(\upsilon^2)} \tag{22}$$

(*e.g.*, Carcione, 2001), where υ for body waves is given in the previous section (equations (12)-(16)), and υ for inter-face waves is given in the next section. The concept of group velocity must be used with caution, since it loses physical meaning for highly anelastic media (Carcione, 2001, p. 145).

DISPERSION EQUATIONS

Ocean overlying the crust

Press and Ewing (1950) and Biot (1952) obtained the dispersion equation for the phase velocity as a function of wavelength (see Ewing *et al.*, 1957, p. 156).

Solution of the problem implies traction-free boundary conditions at the sea surface and continuity of normal stress (pressure in the fluid) and normal displacement at the ocean bottom. The dispersion equation can be expressed as

$$\tan\left(\frac{\omega H}{\upsilon}\sqrt{\frac{\upsilon^2}{\upsilon_{P_1}^2}-1}\right) = \frac{\rho_2 \upsilon_{S_2}^4 \sqrt{\upsilon^2/\upsilon_{P_1}^2-1}}{\rho_1 \upsilon^4 \sqrt{1-\upsilon^2/\upsilon_{P_2}^2}}\left[4\sqrt{1-\frac{\upsilon^2}{\upsilon_{P_2}^2}}\sqrt{1-\frac{\upsilon^2}{\upsilon_{S_2}^2}}-\left(2-\frac{\upsilon^2}{\upsilon_{S_2}^2}\right)^2\right], \tag{23}$$

where 1 denotes the fluid and 2 the solid, υ is the complex velocity of the interface wave, and H is the water depth. The wave system described by equation (23) will be attenuated for complex υ. In the absence of viscoelastic dissipation, the energy loss is associated with refraction of waves from the liquid layer into the solid bottom. For the lossless case and $V_{P_2} > V_{S_2} > V_{P_1}$, which is considered in this work, undamped propagation occurs for

$$I \quad V_{P_2} > V_{S_2} \geq \upsilon \geq V_{P_1}$$

$$II \quad V_{P_2} > V_{S_2} > V_{P_1} \geq \upsilon.$$

The branch of lowest velocity shows a continuous transition between Scholte waves at the ocean bottom and free Rayleigh waves at the crust when going from short wavelengths to long wavelengths (compared to the water depth).

Sediment layer overlying the crust

We solve the dispersion equation in the form obtained by Ewing *et al.* (1957, p. 190). For completeness the dispersion equation is given in the appendix. The difference with Ewing *et al.*'s analysis resides in the inclusion of anelasticity, and therefore, the velocities involved in the dispersion equation are complex and frequency-dependent. The phase velocity of the first mode of the M_1 branch (M_{11}) tends to the velocity of the Rayleigh wave of the half space at long wavelengths, and approaches the velocity of the Rayleigh wave of the layer at short wavelengths. This is the relevant branch regarding the propagation of earthquake Rayleigh waves (Ewing *et al.*, 1957, p. 195). The Stoneley modes at the interfaces are related to the M_2 branch.

MODELING METHOD AND DOMAIN DECOMPOSITION

Wave propagation in the continental crust (and mantle) is modeled using the heterogeneous formulation of the viscoelastic wave equation used by Carcione (1992) to simulate Rayleigh waves for seismic exploration applications. The transition continent-ocean is modeled by using the same formulation and setting the shear modulus of the ocean equal to zero. A domain-decomposition technique is developed and tested to model wave propagation at the ocean bottom. The algorithm is given in detail in the following subsection.

Domain decomposition

We implement a domain-decomposition technique and use the viscoacoustic wave equation to model propagation in the ocean. Two grids model the fluid and the solid subdomains (labeled 1 and 2, respectively). The boundary conditions between subdomains require continuity of

$$\upsilon_z, \sigma_{zz}, \text{ and } \sigma_{xz}(=0). \tag{24}$$

The solution on each of the two grids is obtained by using the Runge-Kutta method for time stepping and the Fourier and Chebyshev differential operators to compute the spatial derivatives in the horizontal and vertical directions, respectively (Carcione, 1992, 1994a, 2001). Chebyshev transforms are computed with the FFT, with a length twice of that used by the Fourier method (Gottlieb and Orszag, 1977). Since the sampling points are very dense at the edges of the mesh, the Chebyshev method requires a one-dimensional stretching transformation to avoid very small time steps (Kosloff and Tal-Ezer, 1993). To combine the two grids, the wave field is decomposed into incoming and outgoing wave modes at the interface between the solid and the fluid. The inward propagating waves depend on the solution exterior to the sub-domains and therefore are computed from the

boundary conditions (24), while the behavior of the outward-propagating waves is determined by the solution inside the subdomain. The approach, given in Carcione (1991), and adapted here for equations (1)-(11), involves the following equations for updating the field variables at the grid points defining the fluid-solid interface:

$$v_x^{(new)}(1) = v_x^{(old)}(1),$$

$$v_z^{(new)} = \left[Z_P(1) + Z_P(2)\right]^{-1}\left[Z_P(2)v_z^{(old)}(2) + Z_P(1)v_z^{(old)} + \sigma^{(old)}(1) - \sigma_{zz}^{(old)}(2)\right]$$

$$\sigma^{(new)} = v_{zz}^{(new)} = \frac{Z_P(1)Z_P(2)}{Z_P(1) + Z_P(2)}\left[v_z^{(old)}(1) - v_z^{(old)}(2) + \frac{\sigma^{(old)}(1)}{Z_P(1)} + \frac{\sigma_{zz}^{(old)}(2)}{Z_P(2)}\right],$$

$$e_1^{(new)}(1) = e_1^{(old)}(1) + \left[\phi_1(1)/k(1)\right]\left[\sigma^{(new)} - \sigma^{(old)}(1)\right],$$

$$v_x^{(new)}(2) = v_x^{(old)}(2) - \sigma_{xz}^{(old)}(2)/Z_S(2),$$

$$\sigma_{xz}^{(new)}(2) = 0,$$

$$\sigma_{xx}^{(new)}(2) = \sigma_{xx}^{(old)}(2) + \frac{k(2) - \mu(2)}{k(2) + \mu(2)}\left[\sigma_{zz}^{(new)} - \sigma_{zz}^{(old)}(2)\right],$$

$$e_1^{(new)}(2) = e_1^{(old)}(2) + \left[\phi_1(2)/k(2) + \mu(2)\right]\left[\sigma_{zz}^{(new)} - \sigma_{zz}^{(old)}(2)\right],$$

$$e_2^{(new)}(2) = e_2^{(old)}(2) - \left[\phi_2(2)/k(2) + \mu(2)\right]\left[\sigma_{zz}^{(new)} - \sigma_{zz}^{(old)}(2)\right],$$

$$e_3^{(new)}(2) = e_3^{(old)}(2) - \left[\phi_2(2)/\mu(2)\right]\left[\sigma_{xx}^{(old)}(2)\right], \tag{25}$$

where $\phi_v = 1/\tau_\sigma^{(v)} - 1/\tau_\epsilon^{(v)}$, $Z_P(1) = \rho_1 V_{P1}$, $Z_P(2) = \rho_2 V_{P2}$, and $Z_S(2) = \rho V_{S2}$. The update is performed at each time step.

The upper boundary of subdomain 1 may satisfy free-surface or non-reflecting boundary conditions (Carcione, 1992: 1994a,b). The free-surface boundary equations are

$$v_x^{(new)} = v_x^{(old)},$$

$$v_z^{(new)} = v_z^{(old)} - \sigma^{(old)}/Z_P,$$

$$\sigma^{(new)} = 0,$$

$$e_1^{(new)} = e_1^{(old)} - \left[\phi_1/k\right]\sigma^{(old)}. \tag{26}$$

The non-reflecting boundary equations are

$$v_z^{(new)} = \frac{1}{2}\left(v_z^{(old)} - \sigma^{(old)}/Z_P\right),$$

$$\sigma^{(new)} = \frac{1}{2}\left(\sigma^{(old)} - Z_P v_z^{(old)}\right),$$

$$e_1^{(new)} = e_1^{(old)} - \left[\phi_1/(2k)\right]\left(\sigma^{(old)} + Z_P v_z^{(old)}\right). \tag{27}$$

The lower boundary of subdomain 2 satisfies non-reflecting boundary conditions (Carcione, 1992, 1994a-b):

$$v_x^{(new)} = \frac{1}{2}\left(v_x^{(old)} + \sigma_{xz}^{(old)}/Z_S\right),$$

$$v_z^{(new)} = \frac{1}{2}\left(v_z^{(old)} + \sigma_{zz}^{(old)}/Z_P\right),$$

$$\sigma_{xx}^{(new)} = \sigma_{xx}^{(old)} - \frac{\left[k(2) - \mu(2)\right]}{2\left[k(2) + \mu(2)\right]}\left(\sigma_{zz}^{(old)} - Z_P v_z^{(old)}\right),$$

$$\sigma_{zz}^{(new)} = \frac{1}{2}\left(\sigma_{zz}^{(old)} + Z_P v_z^{(old)}\right),$$

$$\sigma_{xz}^{(new)} = \frac{1}{2}\left(\sigma_{xz}^{(old)} + Z_S v_x^{(old)}\right),$$

$$e_1^{(new)} = e_1^{(old)} - \left[\phi_1/(2(k + \mu))\right]\left(\sigma_{zz}^{(old)} - Z_P v_z^{(old)}\right),$$

$$e_2^{(new)} = e_2^{(old)} + \left[\phi_2/(2(k + \mu))\right]\left(\sigma_{zz}^{(old)} - Z_P v_z^{(old)}\right),$$

$$e_3^{(new)} = e_3^{(old)} - \left[\phi_2/(2\mu)\right]\left(\sigma_{xz}^{(old)} - Z_S v_x^{(old)}\right). \tag{28}$$

(Note that to obtain the boundary equations for the opposite boundary, say, horizontal boundaries, the method requires the following substitutions: $z \rightarrow -z$, which implies $v_z \rightarrow -v_z$, $\rightarrow -\sigma_{xz}$, and $e_3 \rightarrow -e_3$.) In addition to the non-reflecting conditions, absorbing strips are used to further attenuate the wave field at non-physical boundaries (Carcione, 1992). The damping function is a hyperbolic cosine and the performance is quite acceptable. A better approach would be the perfectly-matched layer method used in electromagnetism (Berenger, 1994). This method is based on a non-physical modification of the wave equation inside the absorbing strips, such that the reflection coefficient at the strip/model boundary is zero.

Scattering

Scattering caused by heterogeneities in the crust and mantle is modeled as variations in the unrelaxed wave velocities. Let ΔV_0 be the maximum deviation of the velocity field from the background value V_0 (P- or S-wave). The velocity field at (x, z) is first subjected to the variations $(\Delta V)^r$, such that

$$-\Delta V_0 \leq (\Delta V)^r \leq \Delta V_0, \tag{29}$$

where $(\Delta V)^r$ is obtained from a 2-D random generator, and the superscript "*r*" denotes random. (Random numbers between 0 and 1 are generated and then scaled to the interval $[-1, 1]\Delta V_0$).

Wave velocity variations in the lithosphere are well described by the von Kármán autocovariance function (Frankel and Clayton, 1986; Holliger, 1997). The corresponding wavenumber-domain power spectrum is

$$P(k_x, k_z) = K(1 + k^2 a^2)^{-(\nu + N/2)}, \tag{30}$$

where $k = \sqrt{k_x^2 + k_z^2}$ is the wavenumber, a is the correlation length, $\nu (0 < \nu < 1)$ is a self-similarity coefficient, K is a

normalization constant, and N is the Euclidean dimension. The von Kármán correlation function describes self-affine, fractal processes of fractal dimension $N + 1 - \upsilon$ at a scale smaller than a.

The velocity is then calculated as

$$V (x, z) = \text{V}_0 \pm \Delta V (x, z), \qquad (31)$$

where

$$\overline{\Delta V}(k_x, k_z) = (\overline{\Delta V})^r (k_x, k_z) P(k_x, k_z), \qquad (32)$$

with $(\overline{\Delta V})^r (k_x, k_z)$ being the Fourier transform of $(\Delta V)^r$ (x, z). (The bar denotes the space Fourier transform.)

To compute consistent random variations of the S-wave velocity (with respect to the P-wave velocity), we use the relation

$$(\Delta V_S)^r (x, z) = \left(\frac{\Delta V_{S0}}{\Delta V_{P0}} \right) (\Delta V_P)^r (x, z).$$

EXAMPLES

In this section, we test the modeling algorithm with an analytical solution, model the Rayleigh-window phenomenon, show examples of wave propagation in the oceanic and continental crusts, and simulate a real earthquake. The properties of water used are $V_{P_1} = 1500$ m/s, $\rho_1 = 1000$ kg/m³, and $Q_{01}^{-1} = 0.0001$.

Comparison with analytical solution

We test the domain-decomposition method by comparing numerical and analytical solutions, with special attention to the simulation of Scholte and leaky Rayleigh waves.

The analytical solution for the fluid-solid plane interface in lossless media is obtained by the method of Cagniard-de Hoop (de Hoop and van der Hijden, 1983; Berg *et al.*, 1994). The two grids, corresponding to the fluid and solid phases, each have 405×81 points with a grid spacing of 1.5 km in the horizontal direction and a vertical size of 90 km (the locations of the closest grid point to the interface are 225 and 115 m for the fluid and solid meshes, respectively). The source is a vertical force applied to the surface of the solid bottom, and has a Ricker wavelet with a dominant frequency of 0.1 Hz. The receiver is located at 300 km from the source and at 115 m below the interface. We consider a hard ocean bottom, which implies a high material contrast at the interface and the presence of a strong leaky Rayleigh wave. The properties of the ocean bottom are $V_{P_2} = 5712$ m/s, $V_{S_2} = 3356$ m/s, and $\rho_2 = 2500$ kg/m³. Solution of the Scholte-wave

dispersion equation (e.g., Brekhovskikh and Lysanov, 1991, p. 67) yields a velocity of 1496 m/s for the Scholte wave and 3091 m/s for the leaky Rayleigh wave. The Runge-Kutta algorithm requires a time step of 0.04 s for stability and accuracy. The numerical and analytical solutions are compared in Figure 1, where it is clear that the agreement is very good.

Figure 2 shows the numerical solutions of the υ_z-component for the elastic (a) and viscoelastic (b) cases (dashed and solid lines, respectively). The viscoelastic ocean bottom has the parameters $Q_{01} = 200$ and $Q_{02} = 100$ at 0.1 Hz. Anelasticity affects the leaky Rayleigh wave more than the other events.

The Rayleigh window

The Rayleigh-window phenomenon has been investigated by Borcherdt *et al.* (1986), who found that the window should be observable in appropriate sets of wide-angle reflection data and that it can be useful in estimating attenuation for various ocean bottom reflectors.

Modeling the Rayleigh window serves to evaluate the performance of the domain-decomposition method in viscoelastic media. We perform a numerical evaluation of the reflection coeficient versus incidence angle from synthetic data generated by the modeling algorithm. The technique has been used by Kindelan *et al.* (1989) for lossless media. Figure 3 shows the comparison of the numerical and analytical P-wave reflection coeficient (a) and phase angle (b) for the oceanic crust defined by $V_{P_2} = 4850$ m/s, $V_{S_2} = 2800$ m/s, $\rho = 2600$ kg/m³, $Q_{01} = 1000$ and $Q_{02} = 10$. The modeling algorithm correctly simulates the Rayleigh-window phenomenon, *i.e.*, the magnitude of the reflection coeficient and phase-change slope. The mismatch between theory (*e.g.*, Carcione, 2001) and numerical experiments is due to the fact that the receivers are located at $h = 1.2739$ m above the interface. Then, there is a phase shift between the incident wave and the reflected wave. At normal incidence, the correction is $\arctan (2h\omega / V_{P_1})$. For a frequency of $f = 20$ Hz and $V_{P_1} = 1480$ m/s, we obtain 12° of phase shift, which coincides with the mismatch observed in Figure 3.

It is difficult to observe the Rayleigh-window phenomenon in the space-time domain, since the reflected pulse is masked by the head wave, because the window is located beyond the S-wave critical angle. The results of Figure 3 constitute a further confirmation of the correctness of the modeling method. To our knowledge, this is the first simulation of this phenomenon by using direct grid methods.

Propagation in the oceanic crust

The physics of wave propagation in the ocean is characterized by the propagation of infinite modes, showing ve-
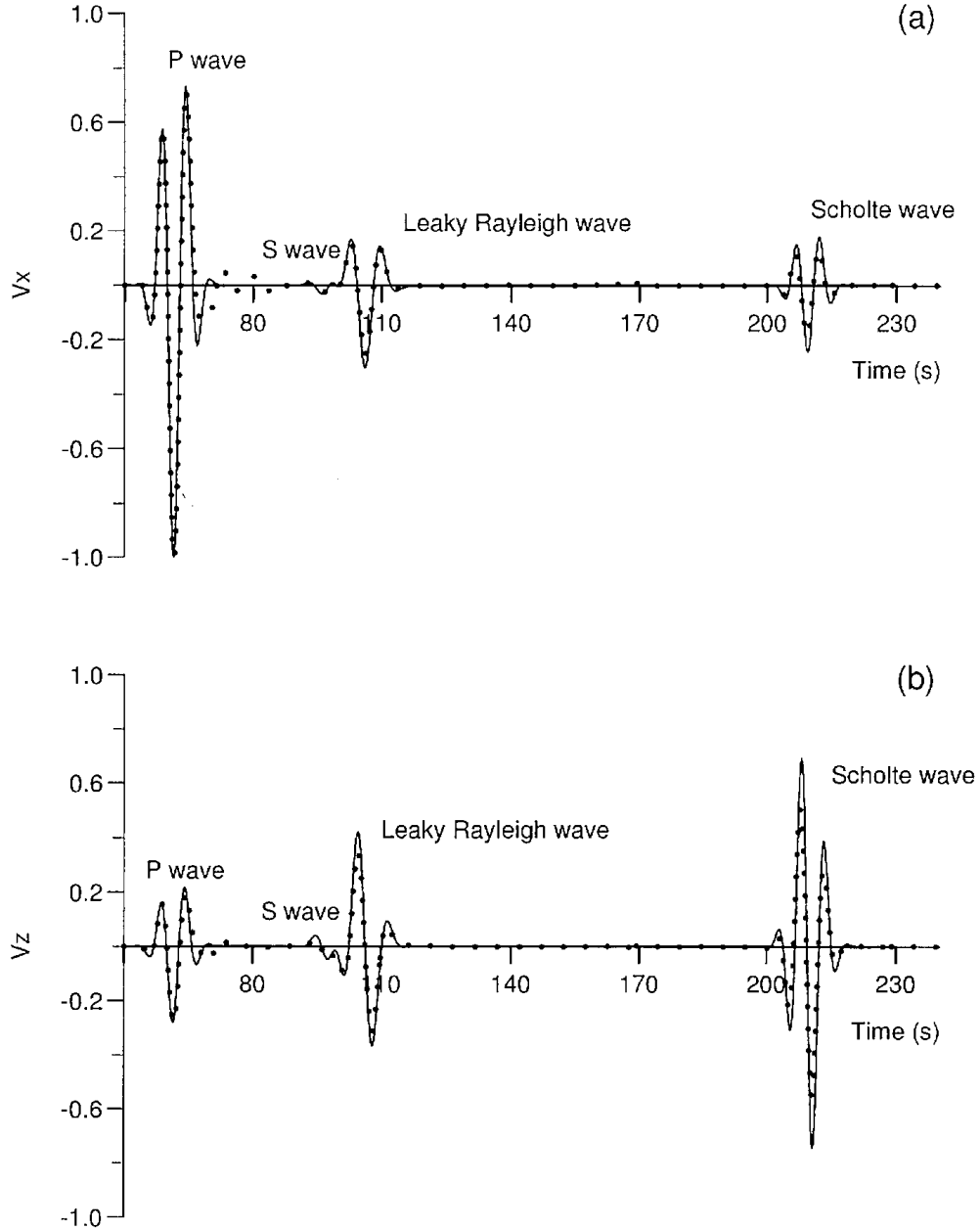
Fig. 1. Numerical and analytical solutions (dots and solid line, respectively) of the v_x-component (a) and v_z-component (b), corresponding to the ocean-bottom interface. The source is a compressional force applied to the solid at 115 m below the interface. The receiver is located at the same horizontal position and at 300 km from the source. The different waves are indicated.

locity dispersion (Biot, 1952). We consider the ocean overlying a solid half space to model the physics illustrated in the previous section. The properties of the ocean bottom used are $V_{P_2} = 5712$ m/s, $V_{S_2} = 3356$ m/s, and $\rho_2 = 2500$ kg/m³.

Figure 4 shows the normalized phase (a) and group (b) velocities of the fundamental mode R_0 (lowest branch) and the next three higher modes R_1, R_2 and R_3 versus the normalized frequency $\gamma = fH/V_{P_1} = H/\lambda$, where $f = \omega/2\pi$ and λ is the wavelength. In the long-wavelength limit ($\gamma \rightarrow 0$), the phase

and group velocities of R_0 tend towards an asymptotic value equal to 3078 m/s = $0.917V_{S_2}$ which is the velocity of the Rayleigh wave traveling along the free surface of the solid half space. The continuous transition between the fundamental mode R_0 and the Scholte wave takes place at $\gamma = 2.162$ where $v_p = V_{P_1}$. The Scholte wave velocity is slightly lower than the speed of sound in water, tending towards an asymptotic value $v_p = 0.997 \, V_{P_1}$ for high frequencies. The higher modes display their characteristic features, starting at $v_p = V_{S_2}$ for the limiting values of γ, corresponding to the onset
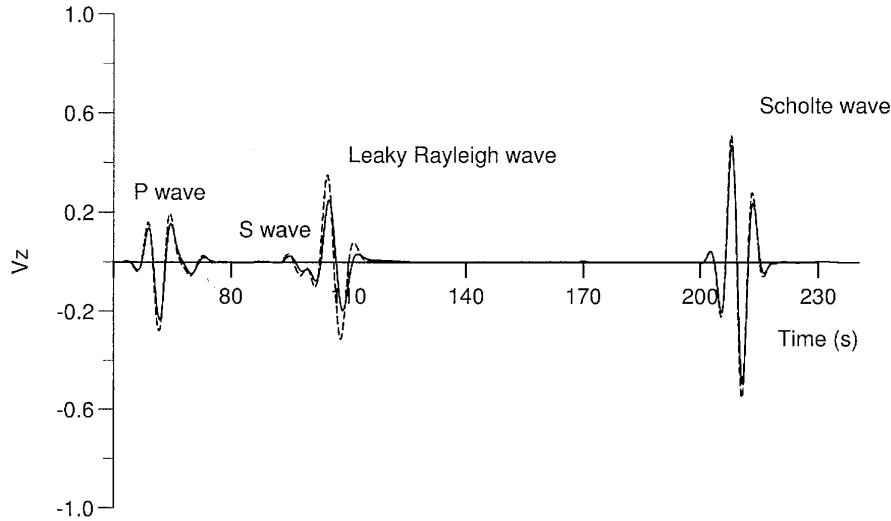
129

Fig. 2. Numerical solutions of the v_z-component for the elastic and viscoelastic cases (dashed and solid lines, respectively). The source is a compressional force applied to the solid at 115 m below the interface. The receiver is located at the same horizontal position and at 300 km from the source. The different waves are indicated.

frequency of the individual mode, and approaching V_{P_1} in the short-wavelength limit ($\gamma \to \infty$). Their group velocity maxima (the Airy phase), on the other hand, gradually decrease with increasing order, which is a common feature observed in real seismograms (*e.g.* Chapman and Staal, 1991; Forsyth, 2000).

The viscoelastic ocean bottom (dashed lines) has the parameters $Q_{01} = 200$ and $Q_{02} = 100$, and the center of the relaxation peaks at $1/\tau 0 = 0.166$ Hz (see equations (13) and (14)), corresponding to $\gamma = 10$ as shown in Figure 4c. The corresponding relaxation peaks for the Rayleigh waves are located at lower frequencies, with their location and value increasing with increasing mode number. Notice that the location of the relaxation peaks (c) coincide with points of maximum curvature of the phase velocity v_p (a), or maximum slope of the group velocity v_g (b). The location of a small peak in the Scholte wave attenuation coincides with that of the body waves.

Consider a comparison of the model predictions with real data. Attenuation of dispersed surface waves traveling along an oceanic path has been analyzed by Ben-Menahem and Singh (1981). Their results show that the attenuation coefficient for the fundamental mode Rayleigh wave, defined by

$$\Gamma = \frac{\pi}{v_g QT} , \qquad (34)$$

where $T = 1/f$ is the wave period, reveals some striking features; a monotonic increase in attenuation is apparent, from $T = 100$ s to a broad maximum centered around $T = 45$ s. Then, a minimum in attenuation at $T = 23$ s is followed by a steep increase towards the short-period range.
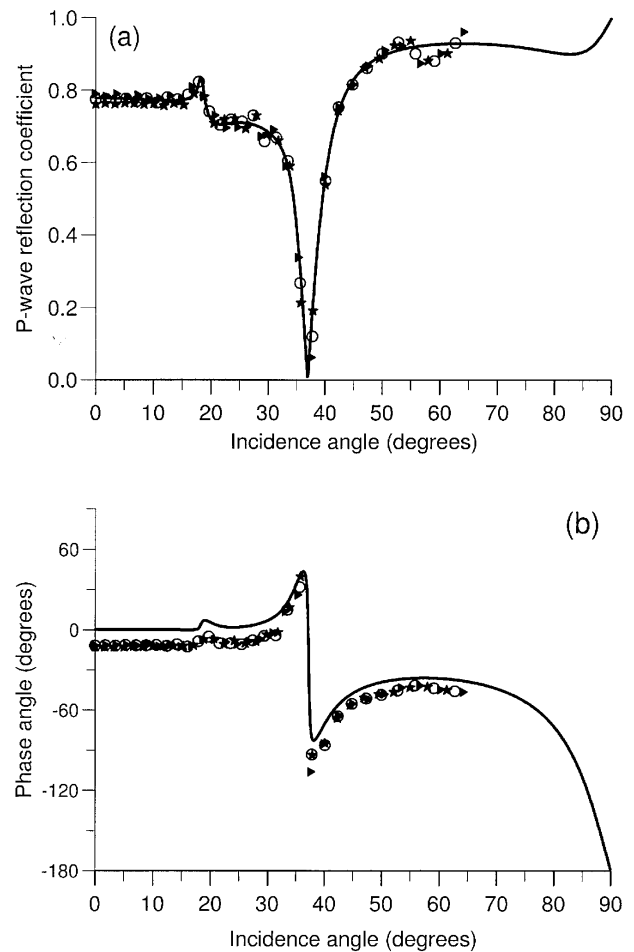

Fig. 3. The Rayleigh window at the ocean-crust interface. P-wave reflection coefficient (a) and phase angle (b) versus incidence angle. The solid line corresponds to the analytical reflection coefficient and the symbols to the numerical evaluation at 18, 19 and 20 Hz.

130

Using their data for the fundamental-mode Rayleigh wave traveling across the Atlantic, from Toledo (Spain) to Trinidad island, we have solved for the corresponding roots of the dispersion equation (23) for the simple two-layer model. Figure 5 shows the attenuation (34), and phase and group velocities obtained for models with ocean depths $H = 5$, 10 and 15 km, respectively. The data of Ben-Menahem and Singh (1981) are shown for comparison. The main fea-

tures from all their observations covering an extended period range, as summarized in their Figure 10.18, are well reproduced in the modeling shown in Figure 5a, using realistic material properties for the solid half-space to match the observed velocities in Figure 5b ($V_{S2} = V_{R0}/0.9$, $V_{P2}=V_{S2} = 1.65$ and $\rho_2/\rho_1 = 2.8$). However, to match their attenuation data, in particular the locations of the attenuation minimum and maximum at 23 and 45 seconds, an unrealistic value of
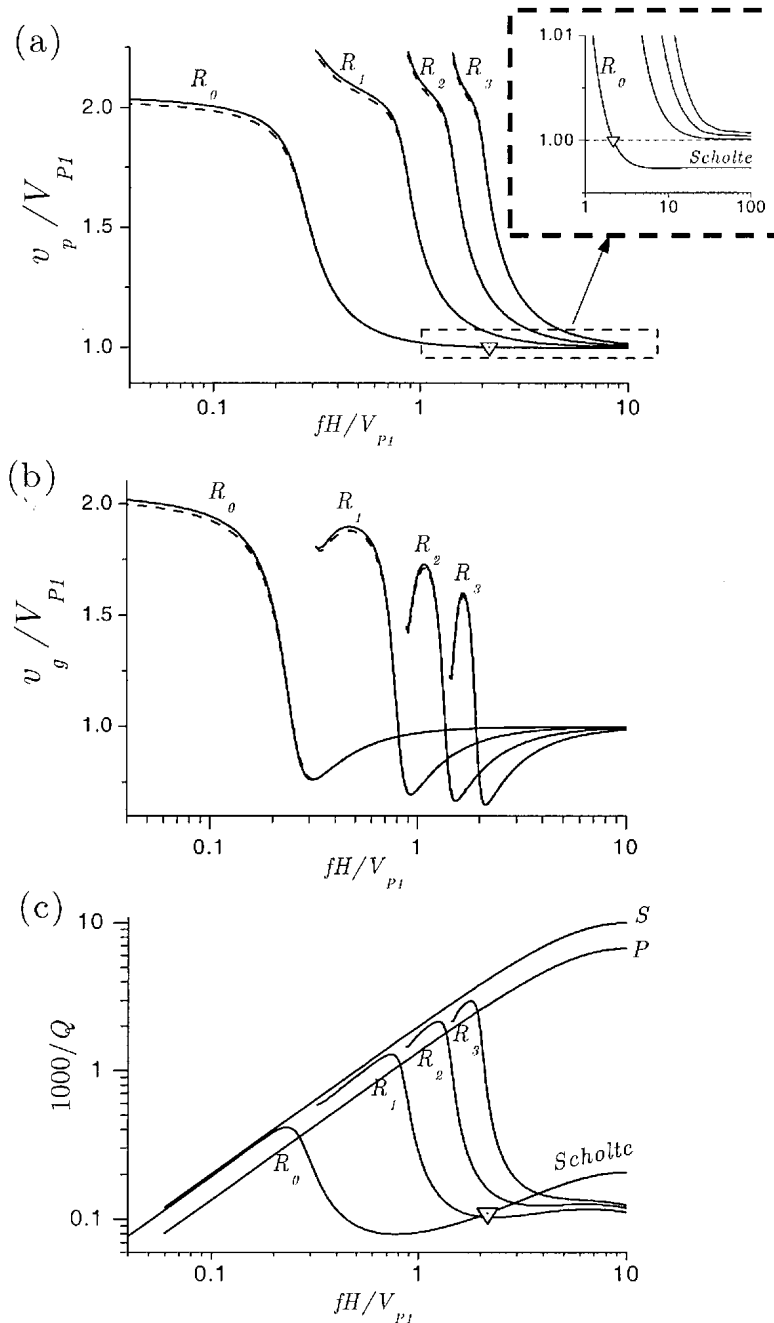
Fig. 4. Normalized phase velocity (a), group velocity (b) and dissipation factor (c) of the fundamental-mode Rayleigh wave R_0 and the three higher modes R_1-R_3 for an elastic (solid line) and anelastic crust (dashed line). The transition (indicated by a triangle) between the fundamental mode R_0 to a Scholte wave is shown in detail in (a). Notice the shift to lower frequencies of the Rayleigh-wave attenuation peaks compared to those of the body waves and Scholte wave (c).
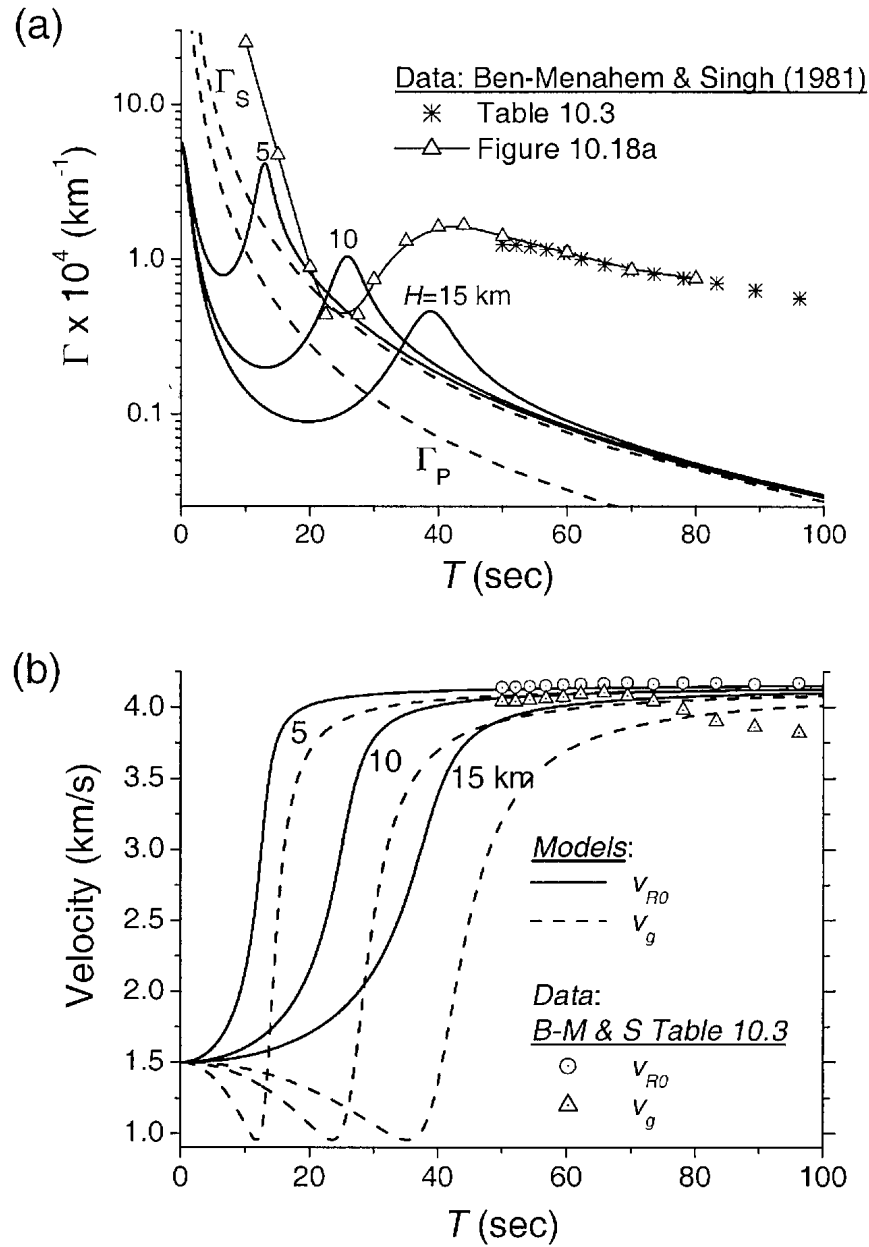
Fig. 5. Theoretical and estimated attenuation coefficient Γ (a) and phase and group velocities (b) for the fundamental-mode Rayleigh wave R_0 using a two-layer model of the wave path across the Atlantic Ocean (Ben-Menahem and Singh, 1981). Results for alternative values of the ocean depth H are shown. Γ_P and Γ_S are the attenuation coefficients for P- and S-waves, respectively, based on the standard linear solid model for viscoelasticity.

the ocean depth of 15 km has to be applied, indicating that the two-layer model is an over-simplification of reality.

Sensitivity to H is also seen in the phase and group velocities in Figure 5b. As in Figure 4, $v_{R0} \rightarrow v_{Scholte}$ for small values of T, with the transition point depending on the value of H ($T = 0.7$, 1.4 and 2.2 sec for $H = 5$, 10 and 15 km, respectively). When $T \rightarrow \infty$, for all values of H, the velocities tend to the velocity of R_0 for the elastic half-space.

Let us now perform the simulation of seismograms using the domain-decomposition modeling method. In the first model, the wavelength of the pulse is much smaller than the water depth (the long-wavelength limit). We consider that the two meshes have 405 × 81 grid points. The horizontal grid spacing is 1.5 km and the vertical size of each mesh is 90 km. (The locations of the closest grid point to the interface are 225 and 115 m for the fluid and solid meshes, respectively). The source location is 2.7 km below the ocean

bottom (sixth grid point), and has a dominant frequency of 0.166 Hz. The water depth to wavelength ratio is 10 (the dominant wavelength in the ocean is 9 km). The traction-free boundary conditions (26) are satisfied at the upper boundary (the sea surface). Forty grid points are used as absorbing boundary at the sides of both meshes and bottom of the lower mesh (in addition to the non-reflecting conditions (27)). The time step of the Runge-Kutta algorithm is 0.06 s. Figure 6 shows a synthetic seismogram of the vertical particle-velocity component, recorded at the ocean bottom, for the lossless case (a), and a comparison between traces at 180 km from

the source for the lossless (dashed line) and lossy (solid line) media (b). The viscoelastic ocean bottom has the parameters $Q_{01} = 200$ and $Q_{02} = 100$. The leaky Rayleigh wave and the shear body wave can hardly be separated in the synthetic traces. The energy of the leaky Rayleigh wave is radiated into the ocean as a head P wave, under the Rayleigh angle (64° with respect to the ocean-bottom interface). This is the reason for the amplitude attenuation with increasing distance. On the contrary, the Scholte wave, being a real root of the dispersion equation, shows no attenuation with increasing distance.
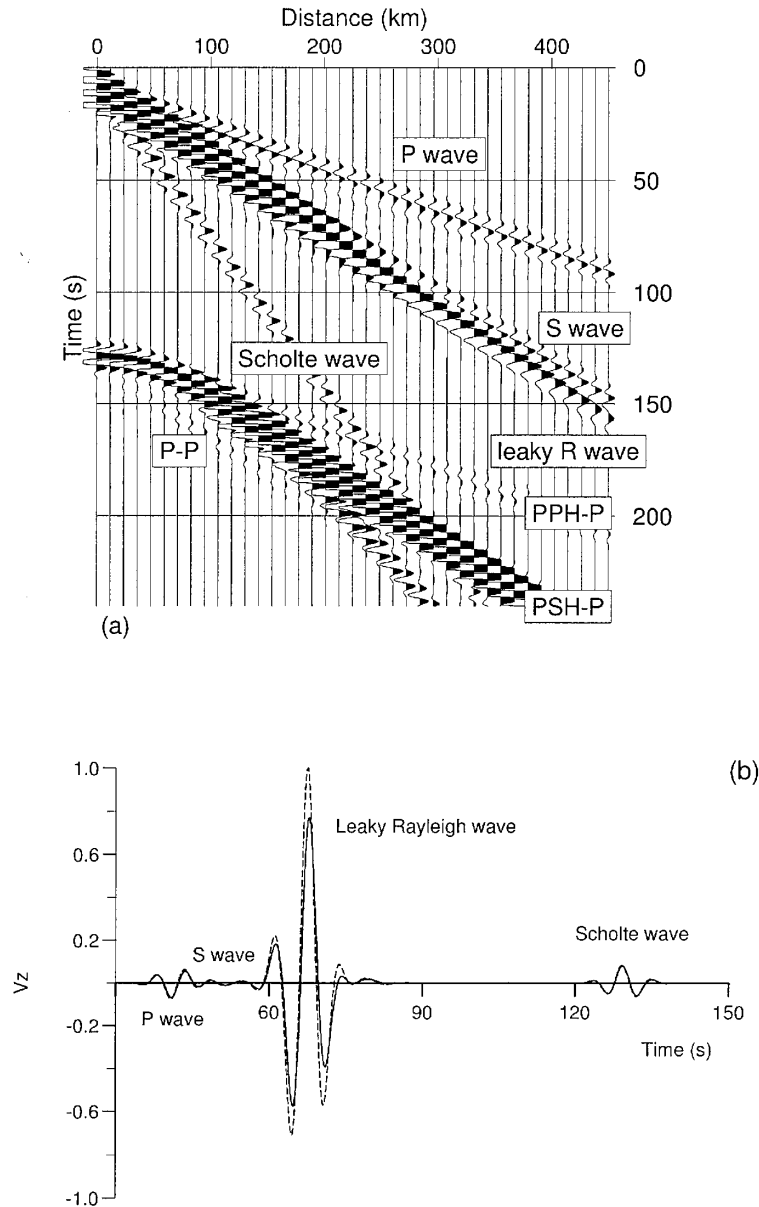

Fig. 6. Synthetic seismogram of the vertical particle-velocity component at the ocean bottom for the lossless case (a), and comparison between traces at 180 km from the source for the lossless (dashed line) and lossy (solid line) simulations. The experiment corresponds to the classical problem solved by Biot (1952) for short-wavelengths. The labeled events are the P wave in the crust (P wave), the S wave in the crust (S wave), the leaky Rayleigh wave (leaky R wave), the Scholte wave, the reflection of the P wave at the ocean surface, and the reflection at the surface of the head wave connecting the P wave in the ocean with the P(S) wave in the crust (PPH-P (PSH-P)).
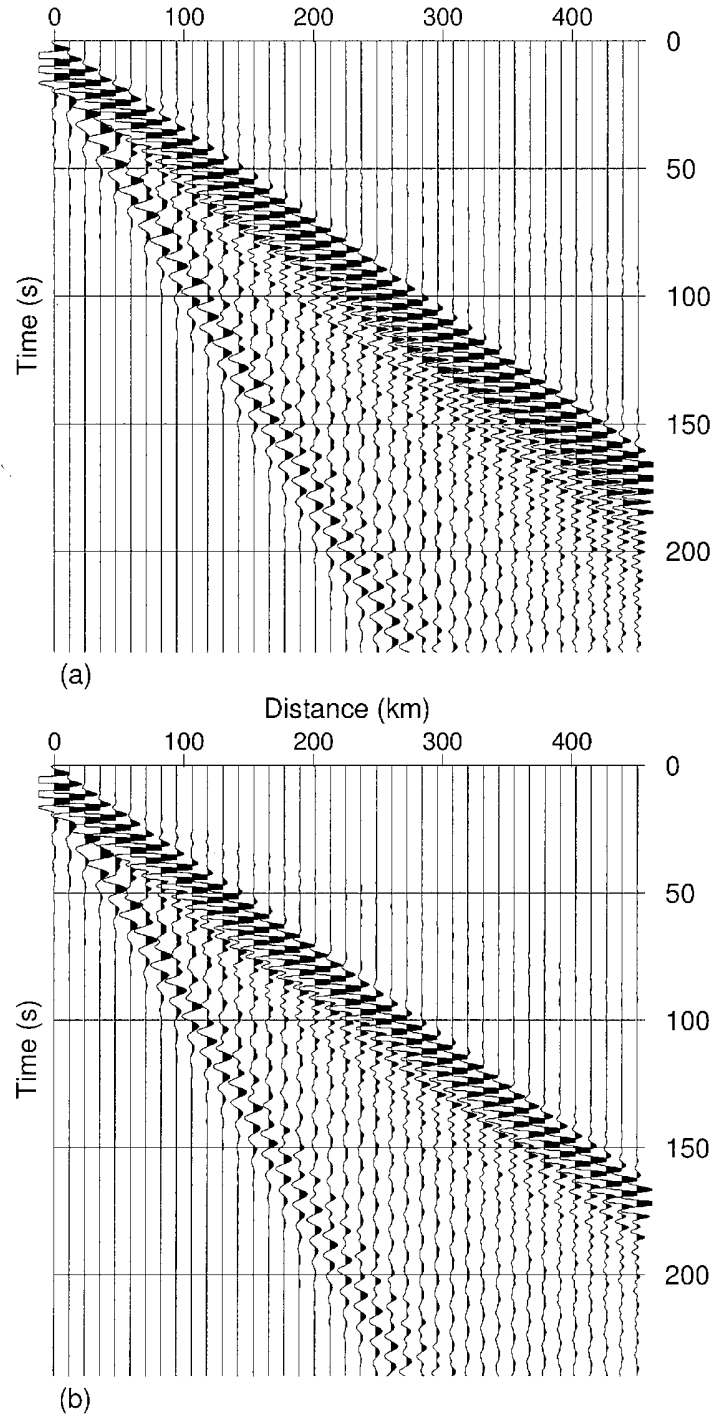
Fig. 7. Synthetic seismograms of the vertical particle-velocity component at the ocean bottom for the lossless (a) and lossy (b) cases. The experiment corresponds to the classical problem solved by Biot (1952) for the long-wavelength limit.

The existence of the leaky wave is subject to the condition that the sound velocity in the liquid must be less than the shear velocity in the solid (this a necessary but not a sufficient condition). The leaky Rayleigh wave approaches the Rayleigh wave as the density of the liquid tends to zero. Hence, the Rayleigh wave in a vacuum solid interface is not a Scholte wave when the density of the liquid goes to zero.

While the free Rayleigh wave always exists, the leaky Rayleigh wave does not (Brower *et al.*, 1979). Most quasi-surface waves, corresponding to roots lying on lower Riemann sheets, are not always physically separable on experimental or numerical simulations because of their close association with body-wave phases. For instance, Phinney (1961) predicts a pseudo-P pulse coupled to the P wave.
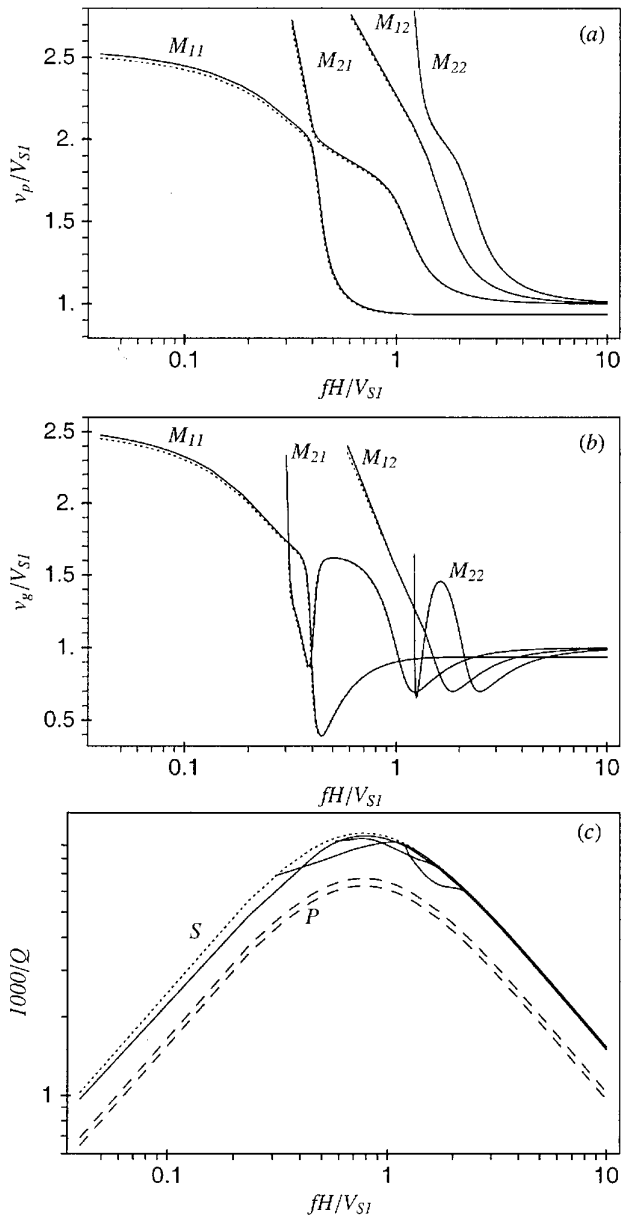
Fig. 8. Normalized phase velocity (a), group velocity (b) and dissipation factor (c) velocities of the fundamental-mode surface wave M_{11} and the three higher modes for an elastic (solid line) and anelastic (dashed line) model of the continental crust. The broken and dotted lines in (c) are the dissipation factors of the P and S body waves, respectively.

For a hard fluid-solid interface, the leaky wave has a velocity slightly lower than the body-wave shear velocity, and the Scholte wave velocity is lower than the liquid sound velocity. As the solid becomes stiffer, the Scholte wave velocity approaches that of the liquid. For soft solids (body-wave shear velocity lower than the sound velocity of the liquid), the leaky Rayleigh-type root is not a physical solution. For the long-wavelength limit, the vertical size of the ocean mesh is 4 km (water depth). The location of the second and

penultimate grid points of the upper mesh are 33 and 65 m, respectively, while the location of the second grid point of the lower mesh is 128 m. In this case, the water depth to wavelength ratio is equal to 0.44 (the dominant wavelength in the ocean is 9 km). Figure 7 shows synthetic seismograms of the vertical particle-velocity component recorded at the ocean bottom for the lossless (a) and lossy (b) cases. The first train of events is a cluster of superimposed wave packets, composed of R_i, $i = 1,..., n$, with the higher frequencies (higher modes) at the tail of the train. These events are Airy phases related to the group velocity maxima (see Figure 4b). The last, low frequency, train of events is related to the Airy-phase minimum of the fundamental mode R_0 ($\gamma = 0.31$) (Figure 4b). This interpretation is also justified by the low attenuation of the latter train compared to the higher attenuation of the first wave train (Figure 4c).

Propagation in the continental crust

To model wave propagation in the continental crust, we consider a sediment layer overlying the crust, modeled as a solid layer overlying a solid half-space. The dispersion equation is given in the appendix. The sediment layer has a thickness of 5.6 km and the following properties: $V_{P_1} = 2500$ m/s, $V_{S_1} = 1200$ m/s, $\rho_1 = 2100$ kg/m^3, $Q_{01} = 200$ and $Q_{02} = 100$. The properties of the crust are $V_{P_2} = 5712$ m/s, $V_{S_2} = 3356$ m/s, $\rho_2 = 2500$ kg/m^3, $Q_{01} = 400$ and $Q_{02} = 500$. Figure 8 shows the normalized phase (a) and group (b) velocities of the fundamental-mode surface wave M_{11} and the three higher modes for an elastic (solid line) and anelastic (dashed line) model. At the low-frequency limit, the velocity of the fundamental mode M_{11} tends to the velocity of Rayleigh waves in the substratum. The other modes tend to the velocity of the shear wave in the substratum. At the high-frequency limit, the velocity of the fundamental mode approaches the Rayleigh-wave velocity in the sediment layer, and the other modes tend to the shear-wave velocity of that layer.

We perform a simulation of an earthquake, where the mesh has 405×101 points with a grid spacing of 1.5 km in the horizontal direction and a vertical size of 106 km. The source is a horizontal force at 7.15 km depth (below the sediment-crust interface), with a central frequency of 0.166 Hz ($\gamma = fH/V_{S_1} = 0.77$). The modeling method developed by Carcione (1992) is used for the simulation and the time step of the algorithm is 0.04 s. Figure 9 shows synthetic seismograms of the horizontal (a) and vertical (b) particle-velocity components, recorded at the surface. A single trace at 300 km from the epicenter is shown in Figure 10. Three wave trains can be distinguished, particularly in the horizontal component. In Figure 10, the first arrival (50 s) is the compressional body wave. Then follows the M_{12} mode (100 s) and the fundamental mode (250 s). The indicated arrival times correspond to the onset of the stronger events. The band-like
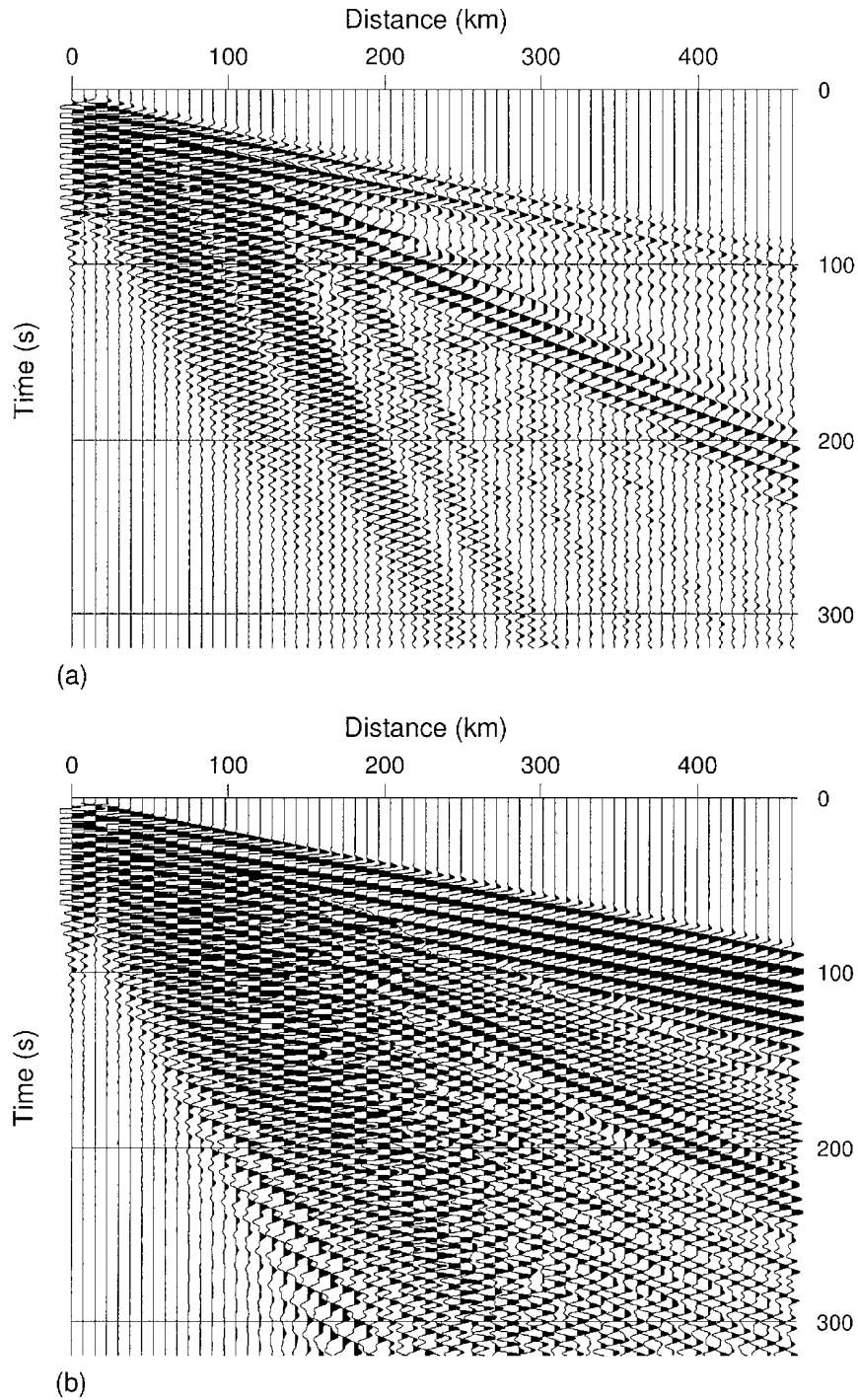
Fig. 9. Synthetic seismograms of the horizontal (a) vertical (b) particle-velocity components corresponding to the continental-crust model.

frequency content of the source implies that the different modes cannot be identified with confidence in the seismograms.

Simulation of an earthquake in the South Atlantic

The modeling algorithm allows us to investigate cases of complex geology, which apply to the propagation of earth-

quake surface waves across the ocean-continent transition and regions of lateral velocity variations. The algorithm developed by Carcione (1992) is used for the following simulation, where the S-wave velocity of water is set to a very small number to preclude the propagation of shear waves in the ocean. The free surface conditions are singular for $V_S = 0$ [see Carcione (1992)]. We simulate the January 7, 2000 earthquake ($M_\omega = 5.5$) recorded at Ushuaia seismograph station

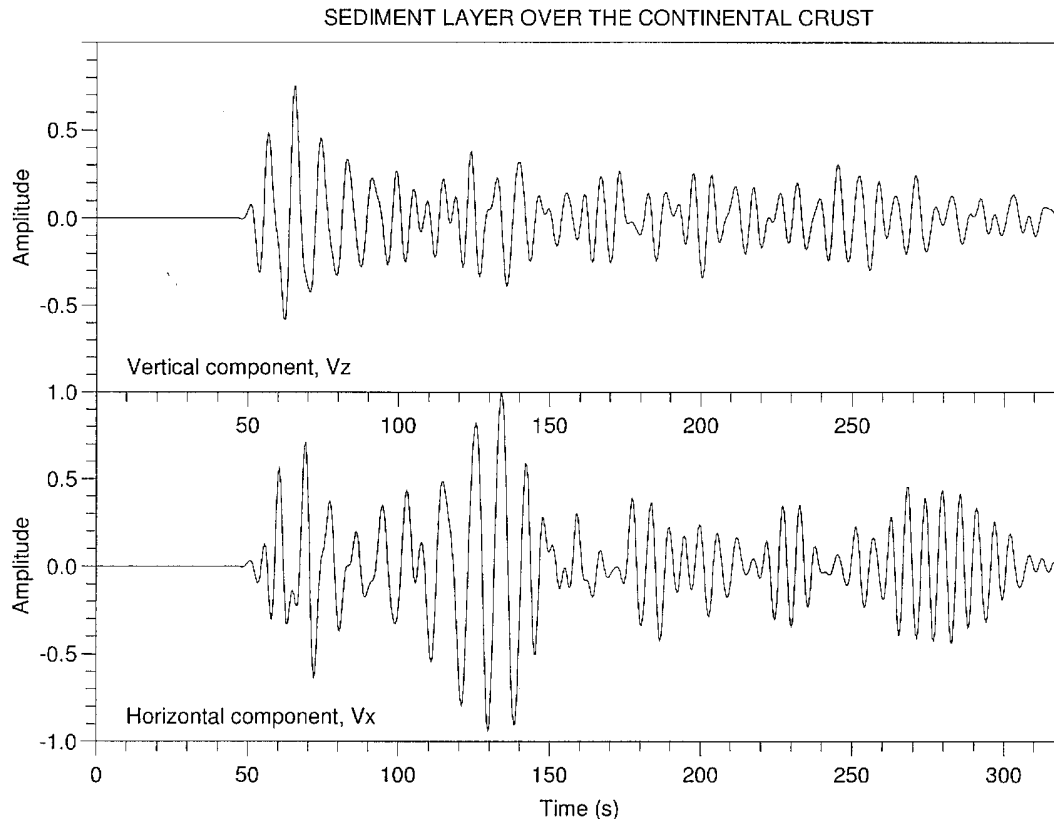SEDIMENT LAYER OVER THE CONTINENTAL CRUST

Fig. 10. Vertical and horizontal seismograms corresponding to the continental-crust model. The distance to the epicenter is 300 km.

(USHU) (Figure 11). The location of the epicenter is indicated by a star, and the source has a depth of 15 km below the sea level (this event is indicated as 010700A in the Harvard CMT Catalog). The real seismograms are shown in Figure 12. Figure 13 shows the two-dimensional model, where the numbers indicate the different layers, whose properties are given in Table 1. The main features of the model have been obtained from lithosphere CRUST 5.1 (Mooney *et al*., 1998) and tomography results published by Vuan *et al*. (2000).

The mesh has 729 × 101 points with a grid spacing of 1.5 km in the horizontal direction and a vertical size of 106.5 km (the location of the closest grid point to the surface is 174 m). The source is a dip-slip moment tensor with components $M_{xx} = -M_0 \sin 2\delta$, $M_{zz} = M_0 \sin 2\delta$ and $M_{xz} = -M_0 \cos 2\delta$, where M_0 is the moment and δ is the dip angle. The rake and strike angles are both equal to $\pi/2$ (e.g., Aki and Richards, 1980, p. 117). Here, we consider $M_0 = 1$ and $\delta = 40°$. The source has a frequency-domain Gaussian function with a peak at 0.2 Hz, and Ushuaia station (the receiver) is located at 870 km from the epicenter. The Runge-Kutta algorithm requires a time step of 0.04 s. Figure 14 shows the simulated horizontal (radial) and vertical components of the wave field. The qualitative aspects of real seismograms are modeled successfully, namely body waves and the fundamental Rayleigh mode. The differences are due to the fact that the numerical

modeling is two dimensional and that the model is not well defined in the study area. We do not intend to obtain a perfect fit between the real and synthetic data, because it is not the aim of this work, and because the 2-D nature of the modeling and the low resolution of the CRUST 5.1 velocity model do not allow such a detailed comparison. Extension of the algorithm to three dimensions, which can be done by using the Fourier pseudospectral method in the *y* direction (Tessmer, 1995), and incorporation of anisotropy, are necessary to improve the simulation. In this sense, the algorithm developed by Tessmer should be generalized to include the effects of wave dissipation.

CONCLUSIONS

We have applied and improved the viscoelastic global pseudospectral modeling algorithm to simulate wave propagation generated by earthquakes, with particular attention to anelastic phenomena. The high accuracy of the modeling has been verified with the analytical solution for a fluid-elastic solid plane boundary, and modeling Scholte waves, leaky Rayleigh waves, and the Rayleigh-window (this constitutes the first simulation of this phenomenon with a direct grid method). The modeling allows for the presence of the sea surface and general material variability along the vertical and horizontal directions.
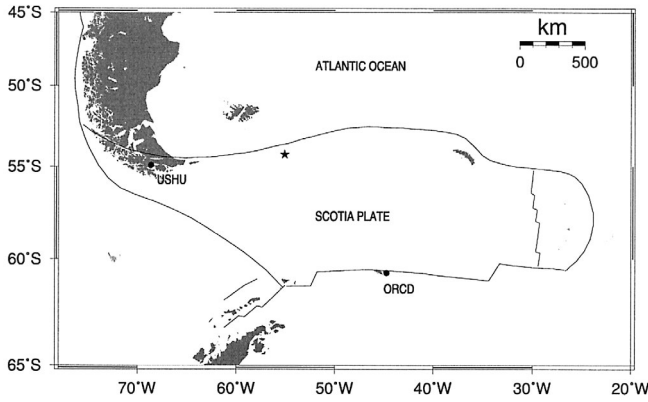
Fig. 11. Location of the epicenter of the January 7 (2000) earthquake (star), and Ushuaia seismograph station (USHU).

Table 1

Properties of the crustal model. (Unrelaxed P- and S-wave velocities, density, P-wave, dilatational and S-wave quality factors, correlation length, maximum P- and S-wave velocity variations and fractal number.)

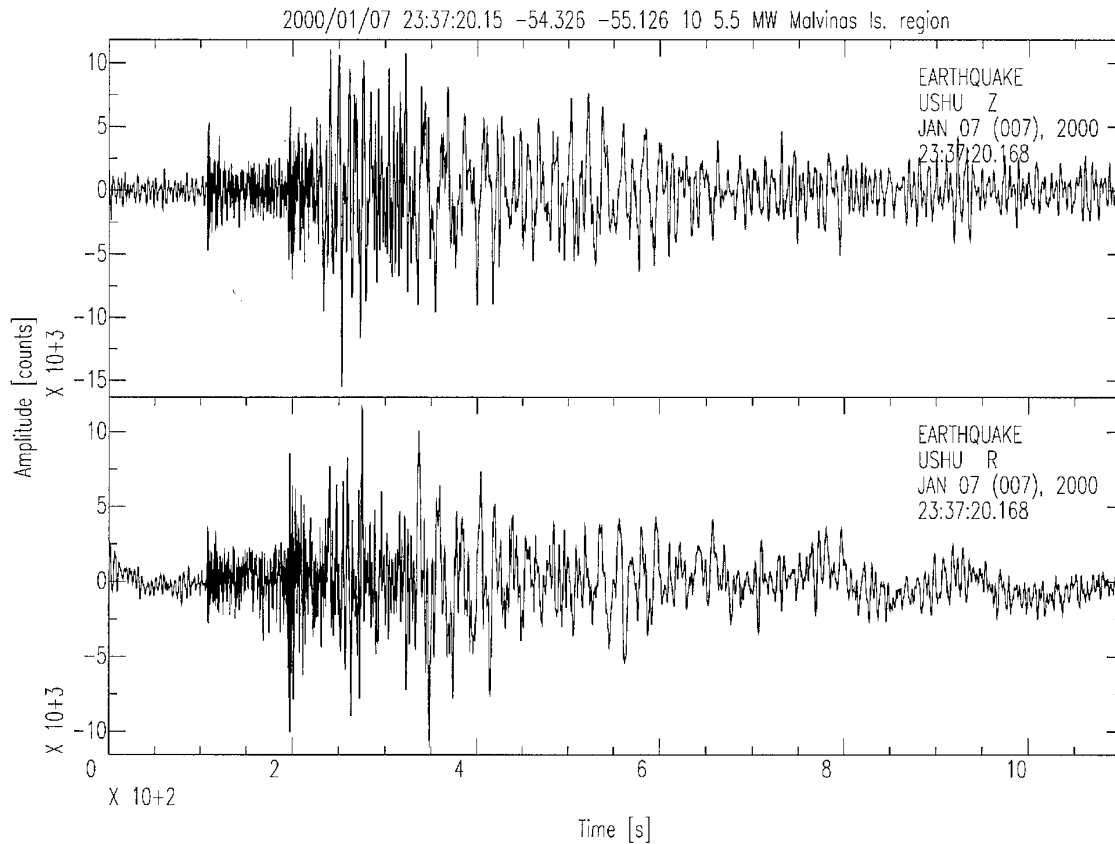| Layer	V_P (km/s)	V_S (km/s)	ρ (g/cm³)	Q_P	Q_{01}	$Q_S(Q_{02})$	a (km)	ΔV_{P0} (km/s)	ΔV_{S0} (km/s)	ν
1	1.5	0	1	10^4	10^4	-	-	-	-	-
2	2.5	1.2	2.1	150	193	100	-	-	-	
3	3.2	1.6	2.3	200	240	150	-	-	-	
4	6	3.4	2.7	400	533	300	4	0.5	0.3	0.15
5	6.6	3.65	2.9	450	636	320	6	0.6	0.4	0.2
6	7.2	4	3.05	500	606	400	8	0.5	0.3	0.18
7	8.1	4.5	3.2	500	606	400	8	0.5	0.3	0.18

Fig. 12. Vertical and radial seismograms of the January 7 (2000) earthquake recorded at Ushuaia station.

This work is a first step towards a complete realistic wave simulation. Ongoing research includes the extension of the modeling algorithm to the three-dimensional anelastic case and anisotropic media, since anisotropy can be important in the upper mantle. The 3-D extension of the algorithm is required to model Love waves (including coupling to Rayleigh waves), and the complete characterization of the earthquake source by the moment-tensor components.
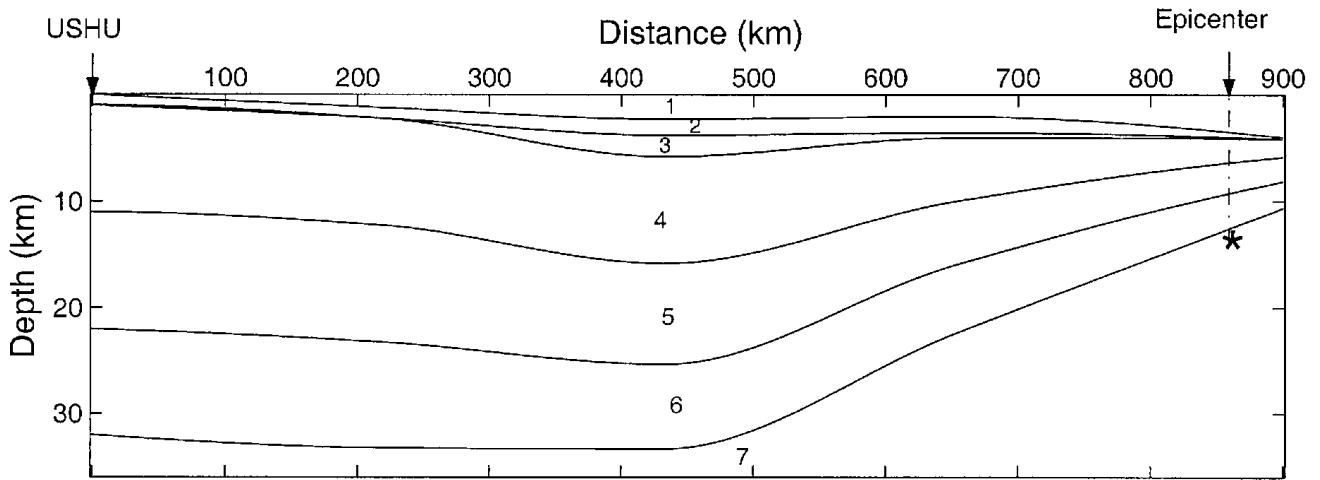
Fig. 13. Geological model at the Scotia Plate to simulate the January 7 (2000) earthquake recorded at Ushuaia station. Layer numbers (1-7) correspond to those of Table 1.
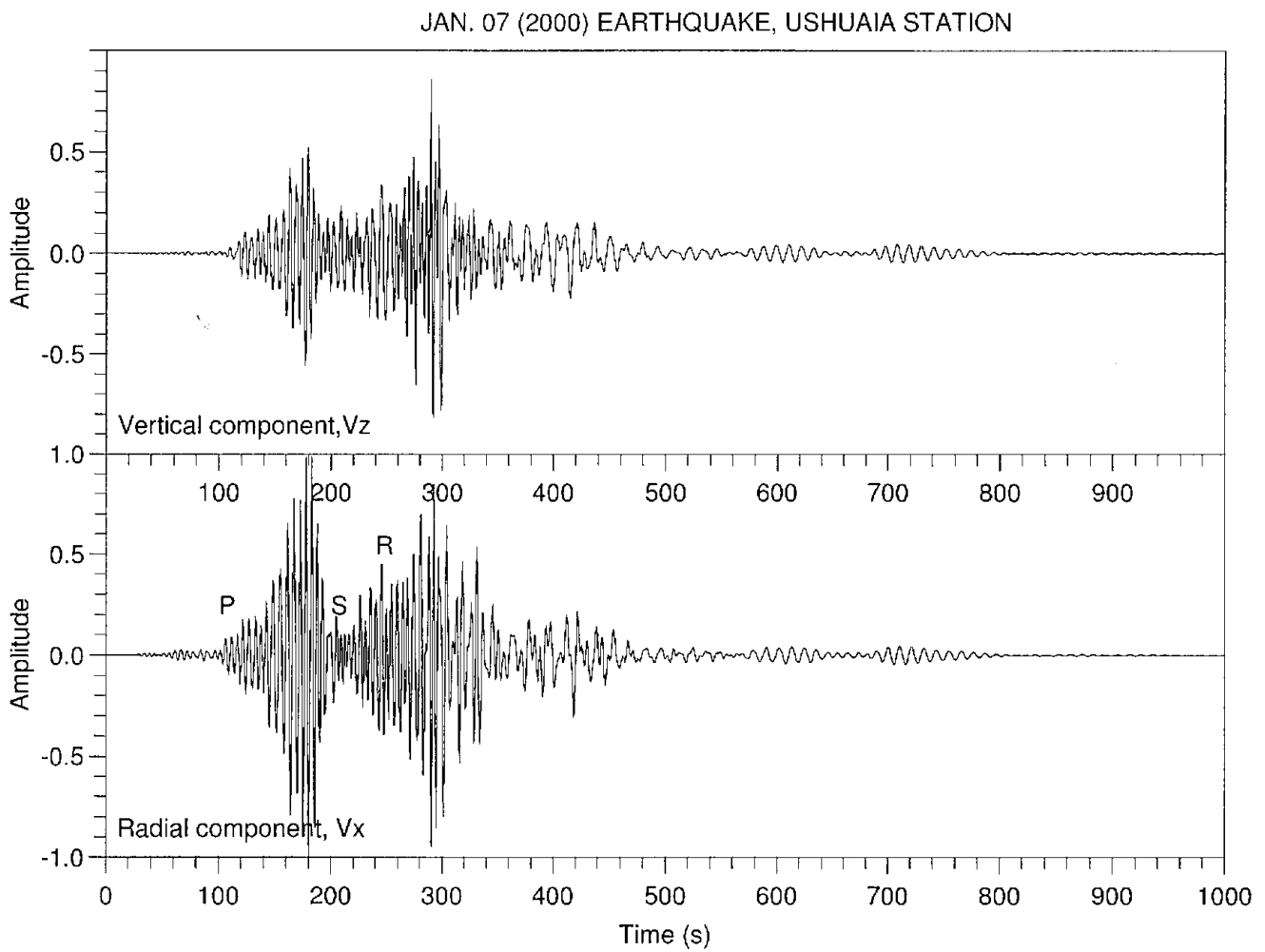

Fig. 14. Simulation of the vertical and radial seismograms of the January 7 (2000) earthquake recorded at Ushuaia station. The labels P, S and R indicate the compressional, shear and Rayleigh waves.

APPENDIX

DISPERSION EQUATION FOR A SOLID LAYER OVER A SOLID HALF-SPACE

Consider a layer of thickness H over a half-space, and define the wavenumbers

$$k_{P_i} = \frac{\omega}{v_{P_i}}, k_{S_i} = \frac{\omega}{v_{S_i}}, v_i = \sqrt{k^2 - k_{P_i}^2}, v_i' = \sqrt{k^2 - k_{S_i}^2}, i = 1,2$$

(A-1)

$$k = \frac{\omega}{v},$$

(A-2)

and

$$\eta = \frac{\rho_2 v_{S_2}^2}{\rho_1 v_{S_1}^2},$$

(A-3)

where v is the complex velocity of the interface wave, and 1 and 2 refer to the layer and half-space, respectively. The dispersion equation results from the boundary conditions, *i.e.*, stress-free conditions at the surface and continuity of stress and displacements at the interface. It is given by

$$
\det \begin{vmatrix}
(2k^2 - k_{S_1}^2)\exp(v_1 H) & 2v_1'\exp(v_1' H) & (2k^2 - k_{S_1}^2)\exp(-v_1 H) \\
2kv_1\exp(v_1 H) & (2k^2 - k_{S_1}^2)\exp(v_1' H) & -2kv_1\exp(-v_1 H) \\
-k & -v_1' & -k \\
-v_1 & -k & v_1 \\
2kv_1 & 2k^2 - k_{S_1}^2 & -2kv_1 \\
2k^2 - k_{S_1}^2 & 2kv_1' & 2k^2 - k_{S_1}^2
\end{vmatrix}
$$

$$
\begin{vmatrix}
-2kv_1'\exp(-v_1' H) & 0 & 0 \\
(2k^2 - k_{S_1}^2)\exp(-v_1' H) & 0 & 0 \\
-v_1' & k & v_2' \\
-k & v_2 & k \\
2k^2 - k_{S_1}^2 & 2kv_2\eta & -\eta(2k^2 - k_{S_2}^2) \\
-2kv_1' & -\eta(-2k^2 - k_{S_2}^2) & -2kv_2'\eta
\end{vmatrix} = 0.
$$

(A-4)

In compact analytical form, this determinant is given by

$$
\begin{aligned}
\det(\bullet) = &-16(2 - s_1^2)\pi_1\sigma_1\Big\{(2 - 2\eta + \eta s_2^2)^2 - 4(1-\eta)^2\pi_2\sigma_2 \\
&- 2(1-\eta)(1-\pi_2\sigma_2)s_1^2 - \eta s_1^2 s_2^2\Big\} \\
&+ (4\pi_1\sigma_1 + (2 - s_2^2)^2)\Big\{-\big[\exp(+\gamma(\pi_1 - \sigma_1)) + \exp(-\gamma(\pi_1 - \sigma_1))\big] \\
&\big[(1-\pi_2\sigma_2)(4 - 4\eta - s_1^2)s_1^2 - (1+\pi_1\sigma_1)((2 - 2\eta + \eta s_2^2)^2 \\
&+ 4(1-\eta)^2\pi_2\sigma_2)\big] \\
&- \exp(+\gamma(\pi_1 - \sigma_1))\eta(2 - \pi_2\sigma_1 + \pi_1\sigma_2)s_1^2 s_2^2 \\
&- \exp(-\gamma(\pi_1 - \sigma_1))\eta(2 + \pi_2\sigma_1 - \pi_1\sigma_2)s_1^2 s_2^2\Big\} \\
&- (4\pi_1\sigma_1 - (2 - s_1^2)^2)\Big\{\big[\exp(-\gamma(\pi_1 + \sigma_1)) + \exp(\gamma(\pi_1 + \sigma_1))\big] \\
&\big[(1-\pi_2\sigma_2)(4 - 4\eta - s_1^2)s_1^2 - (1-\pi_1\sigma_1)((2 - 2\eta + \eta s_2^2)^2 \\
&- 4(1-\eta)^2\pi_2\sigma_2)\big] \\
&+ \exp(-\gamma(\pi_1 + \sigma_1))\eta(2 - \pi_2\sigma_1 - \pi_1\sigma_2)s_1^2 s_2^2 \\
&+ \exp(+\gamma(\pi_1 + \sigma_1))\eta(2 + \pi_2\sigma_1 + \pi_1\sigma_2)s_1^2 s_2^2\Big\}
\end{aligned}
$$

with $\gamma = kH$, and

$$p_i = \frac{v}{v_{P_i}}; \quad s_i = \frac{v}{v_{S_i}}, \quad \pi_i = \sqrt{1 - \left(\frac{v}{v_{P_i}}\right)^2}, \quad \sigma_i = \sqrt{1 - \left(\frac{v}{v_{S_i}}\right)^2}, \quad i = 1,2.$$

(A-5)

BIBLIOGRAPHY

AKI, K. and P. G. RICHARDS, 1980. Quantitative seismology, theory and methods, Vol. 1, W. H. Freeman and Company.

BEN-MENAHEM, A., 1965. Observed attenuation and Q values of seismic surface waves in the upper mantle. *J. Geophys. Res., 70,* 4641-4651.

BEN-MENAHEM, A. and S. J. SINGH, 1981. Seismic waves and sources, Springer-Verlag.

BERENGER, J. P., 1984. A perfectly matched layer for the absorption of electromagnetic waves. *J. Comput. Phys., 114,* 185-200.

BERG, P., F. IF, P. NIELSEN and O. SKOVGAARD, 1994. Analytical reference solutions. *In:* Modeling the Earth for oil exploration, K. Helbig, ed., Pergamon Press, 421-427.

BIOT, M. A., 1952. The interaction of Rayleigh and Stoneley waves in the ocean bottom. *Bull. Seism. Soc. Am., 42,* 81-93.

BORCHERDT, R. D., G. GLASSMOYER and L. WENNERBERG, 1986. Influence of welded boundaries in anelastic media on energy flow, and characteristics of *P*, *S*-I and *S*-II waves: observational evidence for inhomogeneous body waves in low-loss solids. *J. Geophys. Res., 91*, 11503-11118.

BREKHOVSKIKH, L. M. and Y. P. LYSANOV, 1991. Fundamentals of ocean acoustics, Springer-Verlag.

BROWER, N. G., D. E. HIMBERGER and W. G. MAYER, 1979. Restrictions on the existence of leaky Rayleigh waves. *IEEE Trans. on Sonics and Ultrasonics, SU-26*, 306-308.

BUTLER, R. and C. LOMNITZ, 2002. Coupled seismoacoustic modes on the seafloor. *Geophys. Res. Lett., 29*, 57-61.

CAPDEVILLE, Y., E. STUTZMANN and J. MONTAGNER, 2000. Effect of a plume on long-period surface waves computed with normal-mode coupling. *Phys. Earth Plant. Inter., 119*, 54-71.

CARCIONE, J. M., 1991. Domain decomposition for wave propagation problems. *J. Sci. Comput., 6 (4)*, 453-472.

CARCIONE, J. M., 1992. Modeling anelastic singular surface waves in the Earth. *Geophysics, 57*, 781-792.

CARCIONE, J. M., 1994a. Time-dependent boundary conditions for the 2-D linear anisotropic-viscoelastic wave equation, *Numer. Meth. Part. Diff. Equations, 10*, 771-791.

CARCIONE, J. M., 1994b. The wave equation in generalized coordinates. *Geophysics, 59*, 1911-1919.

CARCIONE, J. M., 1996. A 2-D Chebyshev differential operator for the elastic wave equation. *Comput. Methods Appl. Mech. Engrg., 130*, 33-45.

CARCIONE, J. M., 2001. Wave Fields in Real Media. Theory and numerical simulation of wave propagation in anisotropic, anelastic and porous media, Pergamon Press.

CARCIONE, J. M., G. HERMAN and F. P. E. TEN KROODE, 2002. Seismic modeling. G*eophysics, 67*, 1304-1325.

CHAPMAN, D. M. F. and P. R. STAAL, 1991. A summary of DREA observation of interface waves at the seabed. *In*: J.M. Hovem, M.D. Richardson and R.D. Stoll (eds.)

Shear waves in Marine Sediments, Kluwer Academic Publ., 177-184.

COUTEL, F. and P. MORA, 1998. Simulation based comparison of four site-response estimation techniques. *Bull. Seism. Soc. Am., 88*, 30-42.

DE HOOP, A. T. and J. H. M. T. VAN DER HIJDEN, 1983. Generation of acoustic waves by an impulsive line source in a fluid/solid configuration with a plane boundary. *J. Acoust. Soc. Am., 74*, 333-342.

EMMERICH, H. and M. KORN, 1987. Incorporation of attenuation into time-domain computations of seismic wave fields. *Geophysics, 52*, 1252-1264.

EWING, W. M., W. S. JARDETZKY and F. PRESS, 1957. Elastic waves in layered earth, McGraw-Hill Book Co., Inc.

FORSYTH, D. W., 2000. Excitation and propagation of short-period surface waves in young seafloor. *In*: Proceedings of the 22nd Annual DoD/DOE Seismic Research Symposium, New Orleans, 13-15 September, Paper 04-03.

FRANKEL, A. and R. W. CLAYTON, 1986. Finite difference simulations of seismic scattering: implications for the propagation of short-period seismic waves in the crust and models of crustal heterogeneity. *J. Geophys. Res., 91(B6)*, 6465-6489.

GOTTLIEB, D. and S. ORSZAG, 1977. Numerical analysis of spectral methods: Theory and applications, CBMS Regional Conference Series in Applied Mathematics 26, Society for Industrial and Applied Mathematics, SIAM.

HOLLIGER, K., 1997. Seismic scattering in the upper crystalline crust based on evidence from sonic logs. *Geophys. J. Internat., 128*, 65-72.

IGEL, H., 1999. Wave propagation in three-dimensional spherical sections by the Chebyshev spectral method. *Geophys. J. Int., 136*, 559-566.

KESSLER, D. and D. KOSLOFF, 1991. Elastic wave propagation using cylindrical coordinates. *Geophysics, 56*, 2080-2089.

KINDELAN, M., G. SERIANI and P. SGUAZZERO, 1989. Elastic modelling and its application to amplitude versus angle interpretation. *Geophys. Prosp., 37*, 3-30.

KOMATITSCH, and J. TROMP, 2002a. Spectral-element simulations of global seismic wave propagation - I. Validation. *Geophys. J. Int., 149,* 390-412.

KOMATITSCH, and J. TROMP, 2002b. Spectral-element simulations of global seismic wave propagation - II. Three-dimensional models, oceans, rotation and self-gravitation. *Geophys. J. Int., 150,* 303-318.

KOSLOFF, D. and H. TAL-EZER, 1993. A modified Chebyshev pseudospectral method with an $O(N^{-1})$ time step restriction. *J. Comp. Phys., 104,* 457-469.

LOMNITZ, C., R. BUTLER and O. NOVARO, 2002. Coupled modes at interfaces: A review. *Geofís. Int., 41,* 77-86.

MOONEY, W. D., G. LASKE and G. MASTERS, 1998. CRUST 5.1: A global crustal model at 5 degrees by 5 degrees. *J. Geophys. Res., 103(B1),* 727-747.

PHINNEY, R. A., 1961. Propagation of leaking interface waves. *Bull. Seism. Soc. Am., 51,* 527-555.

PRESS, F. and M. EWING, 1950. Propagation of explosive sound in a liquid layer overlying a semi-infinite elastic solid, *Geophysics, 15,* 426-446.

PRIOLO, E., 1999. 2-D spectral element simulation of destructive ground shaking in Catania (Italy). *J. Seismol., 3,* 289-309.

PRIOLO, E., J. M. CARCIONE and G. SERIANI, 1994. Numerical simulation of interface waves by high-order spectral modeling techniques. *J. Acous. Soc. Am., 95,* 681-693.

SERIANI, G., 1998. 3-D large scale wave propagation modeling by a spectral-element method on a Cray T3E multiprocessor. *Comput. Methods Appl. Mech. Eng., 164,* 235-247.

TAKEUCHI, N., R. GELLER and P. CUMMINS, 2000. Complete synthetic seismograms for 3-D heterogeneous Earth models computed using modified DSM operators and their applicability to inversion for Earth structure. *Phys. Earth Plant. Inter., 119,* 25-36.

TESSMER, E., D. KESSLER, D. KOSLOFF and A. BEHLE, 1992. Multi-domain Chebyshev-Fourier method for the solution of the equations of motion of dynamic elasticity. *J. Comput. Phys., 100,* 355-363.

TESSMER, E., 1995. 3-D seismic modelling of general material anisotropy in the presence of the free surface. *Geophys. J. Int., 121,* 557-575.

THOMAS, C., H. IGEL, M. WEBER and F. SCHERBAUM, 2000. Acoustic simulation of P-wave propagation in a heterogeneous spherical earth: numerical method and application to precursor waves to *PKPdf. Geophys. J. Int., 141,* 6441-6464.

VUAN, A., M. RUSSI and G. F. PANZA, 2000. Group velocity tomography in the subantarctic Scotia Sea region. *Pure Appl. Geophys., 157,* 1337-1357.

WINKLER, K. and A. NUR, 1979. Pore fluids and seismic attenuation in rocks. *Geophys. Res. Lett., 6,* 1-4.

ZENER, C., 1948. Elasticity and anelasticity of metals, University of Chicago Press.

José M. Carcione[1], Hans B. Helle[2], Géza Seriani[1] and Milton P. Plasencia Linares[3]

[1] *Istituto Nazionale di Oceanografía e di Geofísica Sperimentale (OGS), Borgo Grotta Gigante 42c,*
34010 Sgonico, Trieste, Italy, Fax: 0039 040 327521
Email: jcarcione@ogs.trieste.it
[2] *Norsk Hydro a.s., 0 & E Research Centre, N-5020 Bergen, Norway; Fax: +47 55 996920*
Email: hans.b.helle@hydro.com
[3] *Departamento de Sismología, Facultad de Ciencias Astronómicas y Geofísicas, Universidad Nacional de La Plata Paseo del Bosque s/n, B1900WA La Plata, Argentina, Fax: 0054 221 4236591*
Email: milton@fcaglp.unlp.edu.ar